

# Generalizable NGP-SR: Generalizable Neural Radiance Fields Super-Resolution via Neural Graph Primitives

Wanqi Yuan  
Clemson University  
wanqiy@clemson.edu

Omkar Sharad Mayekar  
Clemson University  
omayeka@clemson.edu

Connor Pennington  
Clemson University  
cjpenni@clemson.edu

Nianyi Li  
Clemson University  
nianyil@clemson.edu

## Abstract

*Neural Radiance Fields (NeRF) achieve photorealistic novel view synthesis but become costly when high-resolution (HR) rendering is required, as HR outputs demand dense sampling and higher-capacity models. Moreover, naively super-resolving per-view renderings in 2D often breaks multi-view consistency. We propose Generalizable NGP-SR, a 3D-aware super-resolution framework that reconstructs an HR radiance field directly from low-resolution (LR) posed images. Built on Neural Graphics Primitives (NGP), NGP-SR conditions radiance prediction on 3D coordinates and learned local texture tokens, enabling recovery of high-frequency details within the radiance field and producing view-consistent HR novel views without external HR references or post-hoc 2D up-sampling. Importantly, our model is generalizable: once trained, it can be applied to unseen scenes and rendered from novel viewpoints without per-scene optimization. Experiments on multiple datasets show that NGP-SR consistently improves both reconstruction quality and runtime efficiency over prior NeRF-based super-resolution methods, offering a practical solution for scalable high-resolution novel view synthesis. Our project page and code are available at <https://wanqiyuan.github.io/Generalizable-NGP-SR/>.*

## 1. Introduction

Neural Radiance Fields (NeRF) [25] have significantly advanced 3D scene reconstruction and novel view synthesis, enabling photorealistic rendering from sparse 2D images. Follow-up works extended NeRF to support anti-aliased multiscale representations [2, 39, 41], dynamic scene [18, 31, 37], real-time rendering [7, 9, 38], and inverse

rendering[36]. Despite these advances, NeRF’s rendering quality is highly dependent on high-resolution (HR) inputs, and producing HR images is computationally expensive due to dense sampling and large network capacity. A natural solution is super-resolution (SR), which reconstructs high-frequency details from low-resolution (LR) inputs. However, naive 2D SR applied to NeRF renderings often breaks multi-view consistency, leading to artifacts in novel views.

Existing NeRF-based SR methods attempt to mitigate this but face significant limitations. Optimization-based methods [10, 14, 33] often rely on HR reference images, limiting generalization, or struggle to maintain fine-detail consistency. While recent diffusion-based approaches [5, 17] improve perceptual fidelity, they introduce stochastic geometric hallucinations and incur high computational costs, rendering them impractical for real-time applications. Similarly, adaptations of 3D Gaussian Splatting (3DGS) for SR [30, 32] suffer from the overhead of discrete primitives and scalability issues at large magnification factors.

Furthermore, while generalizable NeRF frameworks [8, 21, 22] have emerged to enable fast reconstruction across diverse scenes, they typically prioritize geometry over texture fidelity, resulting in blurred outputs when scaling to high resolutions. This highlights a critical gap: the need for a framework that combines *generalization* with *3D-consistent super-resolution* without the massive overhead of generative foundation models.

In this work, we propose **NGP-SR**, a novel framework that reconstructs high-resolution radiance fields directly from LR inputs and camera poses using Neural Graphics Primitives (NGP). Unlike prior methods that rely on 2D refinement or expensive generative priors, NGP-SR learns high-frequency details directly in 3D space. We achieve this by conditioning the radiance field on **texture tokens** extracted from multi-resolution local feature patches. These tokens provide patch-level context and effectively induce

implicit spatial offsets during radiance evaluation, resembling a multi-sampling behavior that helps recover fine structures while maintaining multi-view coherence. By integrating these token-augmented features within NGP’s efficient hash encoding, our method synthesizes high-fidelity HR renderings with strong generalization to unseen scenes. Our key contributions are:

- We propose **NGP-SR**, a 3D-aware super-resolution framework built on **feature-enhanced Neural Graphics Primitives**, which conditions radiance prediction jointly on spatial coordinates and multi-resolution **local patch texture tokens**.
- We demonstrate that token-conditioned radiance learning can recover high-frequency details while promoting **multi-view consistency** from only LR inputs and camera poses, without requiring HR reference images.
- We show strong **generalization to unseen scenes**, enabling direct HR synthesis for novel viewpoints from LR observations, with improved quality and efficiency over prior NeRF-based SR methods.

## 2. Related Work

**Neural Radiance Fields (NeRF).** Since the introduction of NeRF [25], significant efforts have focused on improving its efficiency and applicability. Works such as Mip-NeRF [2], Zip-NeRF [3], and others [12, 13, 20, 27, 39, 41] tackled anti-aliasing and scale issues. Others extended NeRF to dynamic scenes [23, 28, 31, 37] and real-time rendering [7, 9, 11, 29, 38]. Instant-NGP [26] introduced multi-resolution hash encoding for near-instant reconstruction, while 3D Gaussian Splatting (3DGS) [16] utilized explicit primitives for real-time speeds. To avoid per-scene optimization, generalizable frameworks emerged. MVS-Gaussian [21] and GeFU [22] leverage multi-view stereo and geometry-aware fusion, respectively, while GDB-NeRF [8] utilizes depth-guided bundle sampling. However, these generalizable methods often compromise high-frequency detail for robustness, a limitation our method addresses.

**NeRF Super-Resolution.** NeRF-based SR must recover high-frequency detail while maintaining cross-view consistency, unlike conventional 2D SR [6, 34, 35]. Prior approaches use HR references [14, 33], per-scene latent optimization [10], or diffusion-based refinement [17], often incurring additional supervision, optimization cost, or inference overhead. FastSR-NeRF [19] improves efficiency with lightweight SR modules but is less effective at large magnification. Recent 3DGS SR methods adapt video/2D SR priors [5, 30, 32], but discrete primitives and pretrained priors can introduce overhead and reduce robustness across scenes/resolutions.

**Generalizable NeRFs.** Recent works on generalizable NeRFs aim to reconstruct novel scenes without per-scene optimization. MVS-Gaussian [21] integrates Gaussian splatting with multi-view stereo for fast reconstruction, but its explicit structure struggles to capture fine-grained HR details. GeFU [22] improves quality via geometry-aware fusion and refined rendering, yet still requires scene-specific refinements for consistent HR outputs. GDB-NeRF [8] introduces depth-guided bundle sampling for efficient generalization but does not address super-resolution, leaving high-frequency detail underrepresented. Overall, these methods achieve efficiency and generalization but fall short in producing high-resolution, view-consistent outputs directly from LR inputs—a gap our method addresses.

In contrast, we propose Generalizable NGP-SR, which leverages Neural Graphics Primitives (NGP) to reconstruct high-resolution radiance fields directly from LR inputs and camera poses. By learning high-frequency details in the 3D domain, our framework ensures multi-view consistency, generalizes to unseen scenes, and significantly improves both quality and efficiency compared to existing super-resolution and generalizable NeRF approaches.

## 3. Generalizable NGP-SR Method

Given a set of low-resolution (LR) images  $\{\mathbf{I}_n^{\text{LR}}\}_{n=1}^N$  with corresponding camera poses  $\{\mathbf{C}_n\}_{n=1}^N$ , our goal is to reconstruct a super-resolved radiance field. Once trained, the model can directly synthesize HR outputs for novel viewpoints with camera poses  $\{\mathbf{C}'_m\}$  not seen during training, given only their LR renderings. As illustrated in Fig. 1, our framework consists of three key components: **1) Hierarchical View-Texture Encoding:** Multi-scale LR image patches and their corresponding camera poses are encoded into fixed-length tokens. **2) Camera-Aware Feature Integration:** Camera poses are embedded into the feature generation process, allowing viewpoint-dependent representations that generalize across novel scenes and viewpoints. **3) Global Feature Fusion:** We integrate global LR image features to guide the decoding of HR signals, ensuring multi-view consistency and fine-grained detail.

Our design is inspired by VR-INR [1], which employs hierarchical encoding for video SR. Unlike VR-INR, which operates in purely spatial-temporal domains, our method explicitly incorporates 3D geometry through camera-aware integration and feature fusion, enabling generalizable high-resolution novel view synthesis.

### 3.1. Hierarchical View-Texture Encoding

Given LR input images  $\mathbf{I}_n^{\text{LR}}$  and their associated camera poses  $\mathbf{C}_n$ , our goal is to construct compact, view-aware query tokens that serve as the foundation for 3D-consistent super-resolution.

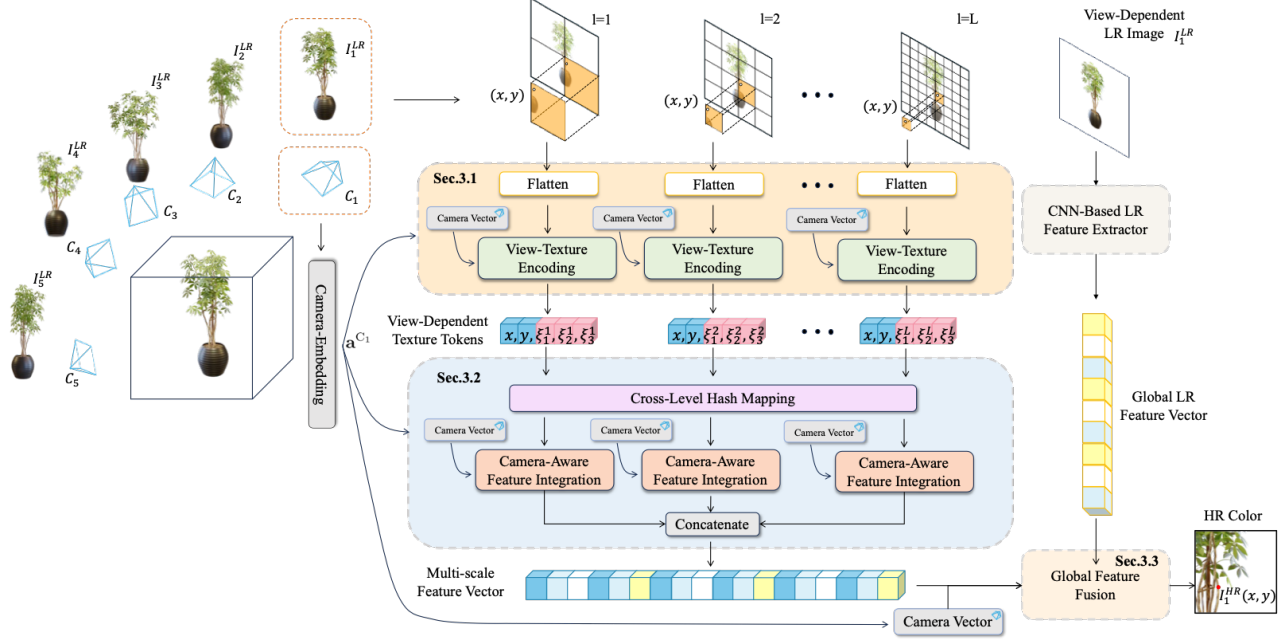


Figure 1. NGP-SR takes low-resolution (LR) images with camera poses and encodes them into hierarchical view-texture tokens that capture local spatial and pose-aware texture cues. These tokens are interpolated through a unified hash table with adaptive, camera-conditioned weights to produce robust multi-resolution feature vectors. Finally, a global feature fusion module integrates holistic LR image context, and a camera-aware decoder synthesizes high-resolution, view-consistent outputs.

At each resolution level  $l$ , we extract local patches containing the HR query coordinates:  $\mathbf{P}_i^l = \mathbf{I}^{\text{LR}}(\mathbf{r}_i^l)$ , where  $\mathbf{P}_i^l$  denotes the sampled patch around location  $\mathbf{r}_i^l$ . These multi-scale patches capture progressively finer spatial context for high-resolution reconstruction, as shown in Fig. 1.

To incorporate viewpoint information, we embed each camera pose  $C_n$  into a latent code via a lightweight MLP:

$$\mathbf{a}^{C_n} = \text{MLP}_a(C_n), \quad (1)$$

which produces a compact representation of the viewing direction. This latent code is injected into the patch encoder  $\mathcal{G}_T^l$  to produce pose-aware texture tokens:

$$[\xi_1^l, \xi_2^l, \dots, \xi_F^l] = \mathcal{G}_T^l(\mathbf{P}_i^l, \mathbf{a}^{C_n}). \quad (2)$$

Finally, hierarchical view-texture query tokens are constructed by concatenating spatial coordinates with the corresponding texture tokens:

$$\mathbf{Q}_{i,n}^l = [\mathbf{x}, \mathbf{y}, \xi_1^l, \dots, \xi_F^l] = [\mathbf{q}_1^l, \dots, \mathbf{q}_S^l]. \quad (3)$$

### 3.2. Camera-Aware Feature Integration

Given the hierarchical view-texture query tokens  $\mathbf{Q}_{i,n}^l$ , our goal is to generate point-wise, view-dependent feature vectors that incorporate both multi-scale spatial context and camera information. This is achieved through a unified hashing and implicit interpolation process.

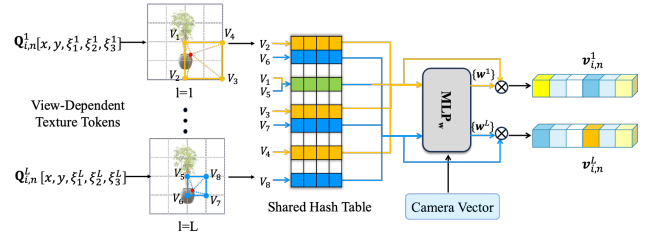


Figure 2. 2D illustration of Cross-Level Hash Mapping mechanism. For each query token, hyper-vertices are identified at multiple resolution levels of the grid. Texture tokens introduce patch-dependent offsets, such that weight of the selected hyper-vertices may differ across resolutions for the same spatial coordinate. To reduce memory consumption, hyper-vertices from coarser levels are mapped to vertices at the finest resolution level.

**Hyper-Vertex Retrieval.** For each query token  $\mathbf{Q}_{i,n}^l$  at resolution level  $l$ , we locate its enclosing hyper-vertices  $\mathbf{V}_{i,n}^l = \{\mathbf{V}_{i,n,k}^l\}_{k=1}^K$  on the discretized multi-resolution grid, where  $K = 2^d$  and  $d$  is the dimension of  $\mathbf{Q}_{i,n}^l$ . Each hyper-vertex  $\mathbf{V}_{i,n,k}^l$  is then mapped to a latent feature vector via a unified hash table:

$$\hat{\mathbf{v}}_{i,n,k}^l = \text{HashTable}(\mathbf{V}_{i,n,k}^l). \quad (4)$$

Unlike level-specific hash mappings, our unified design uses a single shared hash table across all  $L$  levels, significantly reducing memory usage while preserving multi-scale representation. Fig. 2 illustrates such cross-level hash map-

ping in 2D condition.

**Camera-Conditioned Weight Prediction.** To interpolate the hashed features, we predict adaptive weights conditioned not only on the geometric relation of  $\mathbf{Q}_{i,n}^l$  to its surrounding vertices but also on the camera embedding  $\mathbf{a}^{C_n}$ . Specifically, a lightweight two-layer MLP takes as input the relative offset of  $\mathbf{Q}_{i,n}^l$  within its voxel together with  $\mathbf{a}^{C_n}$ , and outputs interpolation weights:

$$[\mathbf{w}_{i,n,1}^l, \dots, \mathbf{w}_{i,n,K}^l] = \text{MLP}_w(\mathbf{Q}_{i,n}^l, \mathbf{a}^{C_n}). \quad (5)$$

**Feature Aggregation.** The final feature vector corresponding to  $\mathbf{Q}_{i,n}^l$  is then computed as the weighted sum of its hyper-vertex features:

$$\mathbf{v}_{i,n}^l = \sum_{k=1}^K \mathbf{w}_{i,n,k}^l \cdot \hat{\mathbf{v}}_{i,n,k}^l. \quad (6)$$

**Multi-Scale Feature Representation.** Repeating this process across all  $L$  resolution levels yields a set of view-dependent feature vectors. Concatenating them forms the final point-wise, multi-scale representation for viewpoint  $C_n$ :

$$\mathbf{v}_{i,n} = [\mathbf{v}_{i,n}^1, \mathbf{v}_{i,n}^2, \dots, \mathbf{v}_{i,n}^L]. \quad (7)$$

### 3.3. Global Feature Fusion

To ensure that high-resolution outputs are both detail-rich and consistent across views, we integrate global low-resolution (LR) image features into the view-dependent feature representations  $\mathbf{v}_{i,n}$ . This is achieved through a two-stage fusion mechanism that combines viewpoint-conditioned features with scene-level global context.

**Stage 1: Camera-Aware Feature Enhancement.** From the previous step, each query point  $\mathbf{Q}_{i,n}$  is represented by its multi-resolution, view-dependent feature vector  $\mathbf{v}_{i,n} = [\mathbf{v}_{i,n}^1, \dots, \mathbf{v}_{i,n}^L]$ . To explicitly encode viewpoint information, we fuse these features with the camera embedding  $\mathbf{a}^{C_n}$ . Specifically, the features and embedding are concatenated and passed through a mapping network  $\mathcal{G}_{\text{cam}}$ :

$$\mathbf{f}_{i,n}^{\text{inter}} = \mathcal{G}_{\text{cam}}(\mathbf{v}_{i,n}, \mathbf{a}^{C_n}), \quad (8)$$

yielding an intermediate representation that encodes both local multi-scale textures and viewpoint cues.

**Stage 2: Global LR Feature Integration.** While  $\mathbf{f}_{i,n}^{\text{inter}}$  captures local and view-dependent details, it lacks holistic scene context. To address this, we extract global image features from the LR input  $\mathbf{I}^{\text{LR}}$  using a CNN-based encoder  $\mathcal{G}_{\text{CNN}}$ :

$$\mathbf{f}_{\text{LR}} = \mathcal{G}_{\text{CNN}}(\mathbf{I}^{\text{LR}}). \quad (9)$$

These global features provide structural and semantic guidance, ensuring that reconstructed HR outputs remain coherent across views.

**Final Fusion.** We then combine the intermediate features  $\mathbf{f}_{i,n}^{\text{inter}}$  with the global LR features  $\mathbf{f}_{\text{LR}}$  through a fusion network  $\mathcal{G}_{\text{fuse}}$ :

$$\bar{\mathbf{v}}_{i,n} = \mathcal{G}_{\text{fuse}}(\mathbf{f}_{i,n}^{\text{inter}}, \mathbf{f}_{\text{LR}}), \quad (10)$$

producing global-context aware feature vectors  $\bar{\mathbf{v}}_{i,n}$  that guide HR reconstruction with both local and global consistency.

**Decoding.** Finally, the fused feature vectors are decoded into HR color values through a two-layer MLP:

$$\hat{\mathbf{C}}_{i,n}^{\text{HR}} = \text{MLP}_c(\bar{\mathbf{v}}_{i,n}). \quad (11)$$

Training is performed by minimizing the pixel-wise Mean Squared Error (MSE) between predictions and ground-truth HR colors:

$$\mathcal{L} = \|\hat{\mathbf{C}}_{i,n}^{\text{HR}} - \mathbf{C}_{i,n}^{\text{HR}}\|_2^2. \quad (12)$$

This global fusion strategy ensures that fine details from local patches are preserved, while structural context from the LR image enforces multi-view coherence across synthesized HR outputs.

## 4. Experiment

### 4.1. Implementation Details

Our framework is implemented in PyTorch, implementation requirement depends on the output resolution. We trained on NVIDIA A100 GPUs with a batch size of 8. We adopt the Adam optimizer with an initial learning rate of 0.00125. The model is trained for  $\geq 200$  epochs/iterations depending on the dataset sizes. Training requires approximately 0.7 hours per scene, while inference achieves 0.7 seconds per image. Detailed implementation requirement will be provided in the supplementary materials.

**Camera Pose Embedding ( $\mathbf{a}^{C_n}$ , Eqn. 1).** We encode each camera pose  $C_n$  into a compact representation using a three-layer MLP. The first two layers have 64 neurons with ReLU activations, followed by a final 16-dimensional output layer with Tanh activation to ensure bounded values in  $[-1, 1]$ .

**Texture Encoder Network ( $\mathcal{G}_T^l$ , Eqn. 2).** For each resolution level  $l$ , the texture encoder is a two-layer MLP that processes vectorized LR image patches. Each hidden layer contains 128 neurons with ReLU activation, and the output is a compact texture code of dimension  $F = 3$ .

**Camera-Aware Mapping Network ( $\mathcal{G}_{\text{cam}}$ , Eqn. 8).** To integrate viewpoint information, we concatenate the multi-resolution feature vector  $\mathbf{v}_{i,n}$  with the camera embedding  $\mathbf{a}^{C_n}$ , and feed the result into a four-layer MLP. Each layer has 64 neurons with Tanh activation. The hidden layers internally allocate 32 dimensions to camera embedding features, ensuring effective fusion between spatial and viewpoint cues.

Table 1. Comparison of SOTAs on Blender datasets with varying resolutions and scaling factors. The best results are highlighted in bold, and the second-best results are underlined.

Methods	Blender×2 (100 × 100)			Blender×4 (100 × 100)			Blender×2 (200 × 200)			Blender×4 (200 × 200)		
	PSNR ↑	SSIM ↑	LPIPS ↓	PSNR ↑	SSIM ↑	LPIPS ↓	PSNR ↑	SSIM ↑	LPIPS ↓	PSNR ↑	SSIM ↑	LPIPS ↓
TensoRF [4]	25.41	0.882	0.161	24.06	0.843	0.188	27.27	0.909	0.199	26.18	0.882	0.146
Instant-NGP [26]	26.34	0.916	0.157	24.83	0.872	0.229	28.29	0.934	0.109	27.07	0.904	0.159
3DGS [16]	27.57	0.935	0.124	25.59	0.887	0.213	29.49	0.949	0.087	27.86	0.916	0.147
LR+Bicubic	28.20	<b>0.946</b>	0.099	25.99	<u>0.896</u>	0.192	30.53	<u>0.962</u>	0.066	28.60	<u>0.927</u>	0.128
NeRF-SR [33]	28.74	0.924	0.066	<u>28.07</u>	<b>0.921</b>	<u>0.071</u>	30.82	0.953	0.055	28.46	0.921	0.076
FastSR-NeRF [19]	27.27	0.902	0.142	22.32	0.453	0.475	31.42	0.952	0.047	<b>30.47</b>	<b>0.944</b>	0.075
SuperGaussian [30]	26.39	0.915	0.090	–	–	–	29.91	0.947	<u>0.035</u>	28.44	0.923	<u>0.067</u>
S2Gaussian [32]	–	–	–	–	–	–	–	–	–	24.19	0.879	0.089
TensoRF+Ours	26.61	0.908	0.093	23.52	0.863	0.119	28.28	0.921	0.068	26.10	0.891	0.103
Instant-NGP+Ours	29.25	<u>0.945</u>	0.062	25.13	0.888	0.098	31.02	0.952	0.041	27.17	0.892	0.085
3DGS+Ours	<b>29.43</b>	<b>0.946</b>	<u>0.051</u>	25.80	0.893	0.085	<u>32.17</u>	0.940	0.041	27.14	0.892	0.076
LR+Ours	<u>29.34</u>	0.938	<b>0.049</b>	<b>28.77</b>	<b>0.921</b>	<b>0.069</b>	<b>33.68</b>	<b>0.971</b>	<b>0.027</b>	<u>29.31</u>	0.923	<b>0.055</b>

Table 2. Comparison of SOTAs on LLFF datasets with varying resolutions and scaling factors. The best results are highlighted in bold, and the second-best results are underlined.

Methods	LLFF×2 (100 × 100)			LLFF×4 (100 × 100)			LLFF×2 (200 × 200)			LLFF×4 (200 × 200)		
	PSNR ↑	SSIM ↑	LPIPS ↓	PSNR ↑	SSIM ↑	LPIPS ↓	PSNR ↑	SSIM ↑	LPIPS ↓	PSNR ↑	SSIM ↑	LPIPS ↓
TensoRF [4]	24.07	0.754	0.314	22.16	0.591	0.596	24.69	0.750	0.309	23.49	0.648	0.503
Instant-NGP [26]	22.17	0.667	0.335	20.90	0.543	0.479	21.47	0.616	0.332	20.81	0.571	0.428
3DGS [16]	23.20	0.735	0.307	21.52	0.581	0.580	23.76	0.748	0.294	22.73	0.654	0.478
LR+Bicubic	24.56	0.765	0.299	22.62	0.608	0.579	25.92	0.793	0.260	24.43	0.687	0.468
NeRF-SR [33]	26.24	0.838	<u>0.123</u>	24.07	0.713	0.252	<u>27.15</u>	0.837	<u>0.122</u>	25.44	0.745	0.208
FastSR-NeRF [19]	24.33	0.765	0.297	21.20	0.584	0.473	26.21	0.822	0.241	21.30	0.384	0.475
3DSR [5]	26.38	<u>0.886</u>	0.181	24.18	<u>0.760</u>	0.342	24.90	<u>0.838</u>	0.235	<u>25.88</u>	<u>0.809</u>	0.261
S2Gaussian [32]	–	–	–	–	–	–	–	–	–	20.45	0.654	<u>0.139</u>
TensoRF+Ours	<u>26.46</u>	0.805	0.181	<u>25.34</u>	0.751	0.190	27.07	0.809	0.170	24.49	0.718	0.213
Instant-NGP+Ours	23.31	0.719	0.171	22.30	0.689	0.206	21.74	0.646	0.155	20.92	0.588	0.264
3DGS+Ours	26.11	0.805	0.168	25.07	0.754	<u>0.183</u>	26.87	0.828	0.149	25.42	0.749	0.176
LR+Ours	<b>30.32</b>	<b>0.892</b>	<b>0.072</b>	<b>29.29</b>	<b>0.847</b>	<b>0.112</b>	<b>32.90</b>	<b>0.934</b>	<b>0.040</b>	<b>29.61</b>	<b>0.874</b>	<b>0.074</b>

**Global Feature Extractor ( $\mathcal{G}_{\text{CNN}}$ , Eqn. 9).** Global context is captured using a lightweight CNN with three convolutional layers ([64, 64, 32] channels),  $3 \times 3$  kernels, and ReLU activations. An adaptive average pooling layer produces a 32-dimensional global feature vector.

**Two-Stage Fusion Network ( $\mathcal{G}_{\text{fuse}}$ , Eqn. 10).** The fusion module first combines hierarchical features and camera embeddings via a four-layer MLP (64 neurons, Tanh activations). The intermediate fused representation is then merged with global LR features in a second four-layer MLP of the same configuration. Both stages use intermediate embeddings of size 32 for efficient integration of local and global information. For clarity and completeness, additional implementation details are provided in the supplementary materials.

## 4.2. Comparison Experiments

**Benchmarks and Protocol.** We evaluate our approach on three widely used datasets for novel view synthesis (NVS) and super-resolution. **Blender**[25]: 8 synthetic scenes with diverse shapes and materials. We train on the training sets

and evaluate on the held-out, unseen test sets of all eight scenes. Input images are downsampled to  $100 \times 100$  and  $200 \times 200$ , and results are reported for SR scales of  $\times 2$  and  $\times 4$ . **LLFF**[24]: eight forward-facing real-world scenes. Following NeRF-SR [33], we train on the entire dataset due to the limited number of images per scene. Evaluation is conducted on SR novel views synthesized by different NeRF backbones. **DTU** [15]: a multi-view stereo benchmark with 124 indoor scenes captured under seven lighting conditions. We use 88 training scenes with  $128 \times 128$  LR inputs and  $\times 4$  SR, and evaluate on 8 held-out DTU test set. **Metrics.** We employ standard metrics, including Peak Signal-to-Noise Ratio (PSNR), Structural Similarity Index Measure (SSIM), and Learned Perceptual Image Patch Similarity (LPIPS) [40], to comprehensively assess pixel accuracy, structural fidelity, and perceptual quality of SR results. For methods without SR, their outputs are bicubically upsampled to match target resolution. We also report *LR+Ours* (downsampled HR ground-truth as LR input, super-resolved with ours) to indicate the attainable upper bound of our framework.

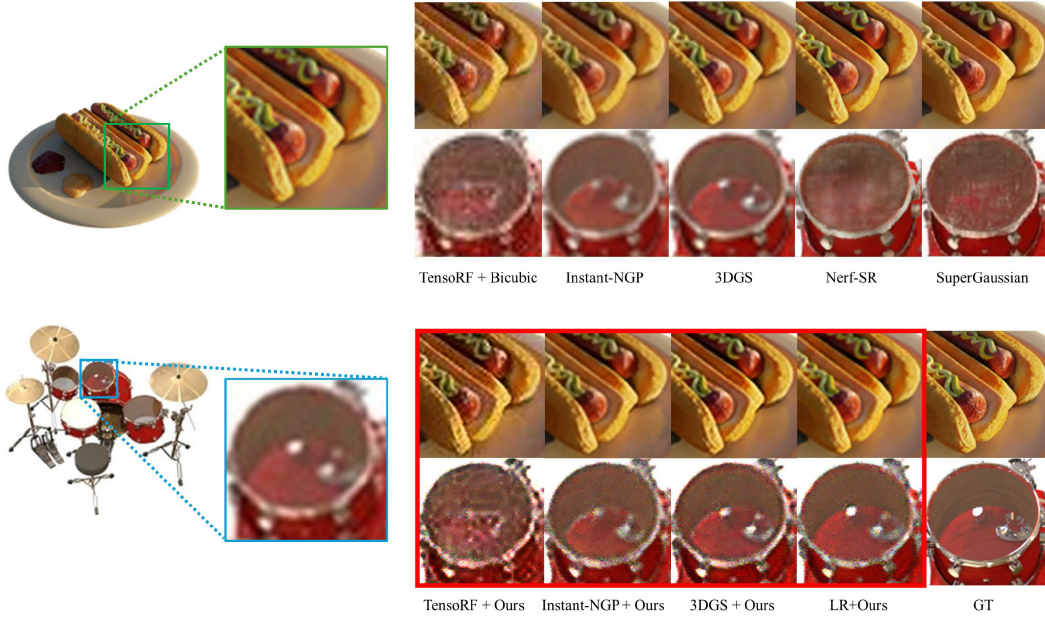


Figure 3. The qualitative comparison of our method on the Blender datasets, with input images at  $200 \times 200$  resolution and  $\times 4$  super-resolution. The leftmost images show the low-resolution inputs, while the images highlighted in red correspond to our results. Compared with other methods that fail to recover fine structures, our approach successfully reconstructs sharp and detailed results. Notably, our method consistently enhances regions where other approaches produce blurred or low-frequency reconstructions.

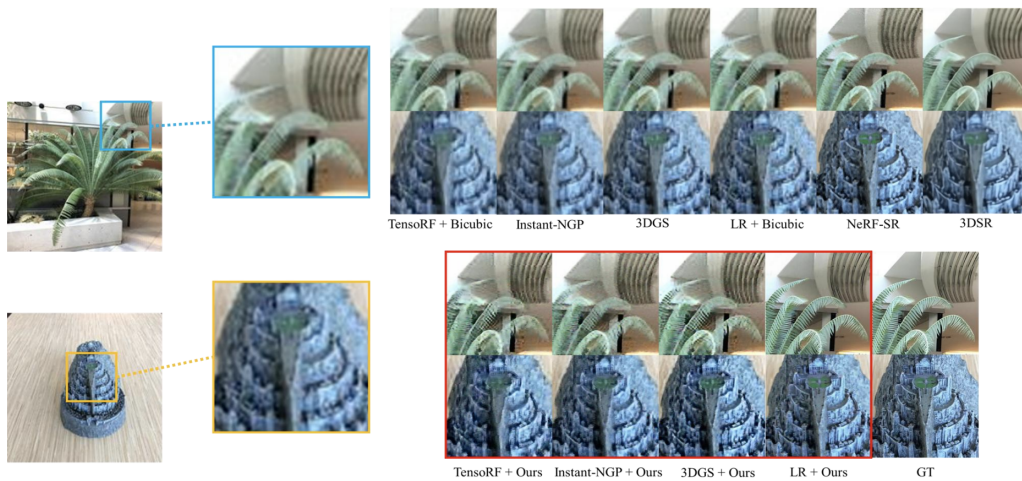


Figure 4. The qualitative comparison of our method on the LLFF datasets, with input images at  $200 \times 200$  resolution and  $\times 4$  super-resolution. The leftmost images show the low-resolution inputs, while the images highlighted in red correspond to our results. Our method successfully reconstructs fine details in leaves and architectural structures, and consistently improves reconstruction quality in regions where other methods exhibit degraded results.

**Compared Methods.** We group baselines into three categories: 1) *Backbone-only NVS without SR*: TensorRF [4], Instant-NGP [26], and 3D Gaussian Splatting (3DGS) [16]. Since these methods do not perform SR, we upsample their LR outputs using bicubic interpolation ( $\times 2$ ,  $\times 4$ ). 2) *NeRF-based SR*: NeRF-SR [33] and FastSR-NeRF [19]. Both re-

quire HR reference supervision, which limits their applicability in low-resolution only settings. As FastSR-NeRF is not open-sourced, we directly report the numbers from their paper; hence, no visual comparison is available. 3) *3DGS + video SR*: SuperGaussian [30], which adapts pretrained video SR models to upsample continuous 3DGS renderings.

Since results on the LLFF dataset are not provided, we only compare against SuperGaussian on Blender (Tab. 1). For S2Gaussian [32], since the authors do not provide publicly available code, we directly report the results as presented in the original paper. And 3DSR [5] on LLFF dataset. 4) *Generalizable NeRFs*: MVSGaussian [21], GeFU [22], and GDB-NeRF [8], evaluated on DTU with input images resized to  $512 \times 512$ .

**Quantitative and Qualitative Analysis.** Tables 1, 2, and 3 summarize quantitative results, and Figures 6, 3 and 4, and provide visual comparisons. Backbone-only NVS methods degrade severely at extreme low-resolution inputs ( $100 \times 100$  and  $200 \times 200$ ), in many cases performing worse than bicubic upsampling. This is due to the reduced number of rays and the strong ambiguity of LR observations, which prevent accurate high-frequency reconstruction. In contrast, when combined with our NGP-SR, NeRF and 3DGS backbones achieve significant improvements across all metrics, demonstrating the effectiveness of our framework as a modular SR component. On Blender, our method outperforms both NeRF-SR and FastSR-NeRF at extremely low resolutions ( $100 \times 100$ , despite their reliance on HR references, while also surpassing SuperGaussian and in most cases. On LLFF, NGP-SR achieves especially strong performance, which can be attributed to training on all images per scene—similar to NeRF-SR, and the tendency of our NGP-based interpolation to overfit more effectively to observed views. This property allows NGP-SR to reconstruct high-fidelity details when test views share similar content with the training set. On DTU, NGP-SR generalizes well to unseen test scenes, producing sharper details and more consistent reconstructions from LR inputs and camera poses.

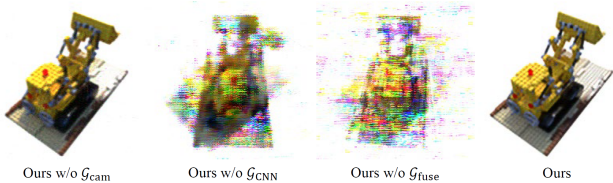


Figure 5. Quantitative ablation on the Lego scene.

## 5. Ablation Study

We conduct comprehensive ablation studies to analyze the contributions of key components in our framework. To systematically assess the effectiveness of these modules, we create subnetworks by individually removing each component and report both qualitative and quantitative outcomes on the Lego scene from the Blender dataset, using a resolution scale factor of  $\times 2$  and input resolution of  $100 \times 100$ .

Table 3. Comparison of SOTAs on DTU datasets with  $512 \times 512$  resolution.

Methods	DTU		
	PSNR $\uparrow$	SSIM $\uparrow$	LPIPS $\downarrow$
MVSGaussian	21.95	0.863	0.112
GeFU	23.15	0.880	<b>0.100</b>
GDB-NeRF	22.42	0.867	0.111
Ours ( $\times 4$ )	<b>31.38</b>	<b>0.884</b>	0.122

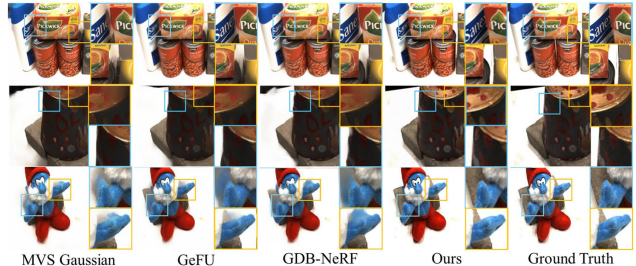


Figure 6. Qualitative evaluation of novel-scene generalization on the DTU dataset. Each panel shows the reconstructed image (left) and two zoomed-in crops (right). Baselines use  $512 \times 512$  inputs, while our method operates on  $128 \times 128$  inputs with  $\times 4$  super-resolution and still reconstructs sharp details with accurate lighting.

Table 4. Ablation studies of our method on the Lego dataset using PSNR, SSIM, and LPIPS metrics.

Methods	Lego $\times 2$ ( $100 \times 100$ )		
	PSNR $\uparrow$	SSIM $\uparrow$	LPIPS $\downarrow$
Ours w/o $\mathcal{G}_{cam}$	26.69	0.892	0.082
Ours w/o $\mathcal{G}_{CNN}$	13.38	0.538	0.471
Ours w/o $\mathcal{G}_{fuse}$	13.69	0.585	0.436
Ours	<b>30.60</b>	<b>0.952</b>	<b>0.075</b>

Results are summarized in Table 4 and qualitatively illustrated in Figure 5.

**Camera-Aware Mapping Network ( $\mathcal{G}_{cam}$ )** This module integrates view-dependent feature vectors with camera pose embeddings via an MLP, enabling robust viewpoint adaptation. For ablation, we replace  $\mathcal{G}_{cam}$  with a simpler two-layer MLP without camera pose conditioning. The resulting model suffers a notable performance drop (PSNR: -3.27 dB, SSIM: -0.053, LPIPS: +0.02), confirming the critical role of explicit camera pose embedding.

**Global Feature Extractor ( $\mathcal{G}_{CNN}$ )** This component captures structural and textural context from low-resolution inputs. Ablating this module significantly degrades reconstruction quality (PSNR: -16.58 dB, SSIM: -0.407, LPIPS: +0.409), demonstrating its importance in providing global context. Qualitative results in Figure 5 highlight clear fail-

ures in texture and pose reconstruction when  $\mathcal{G}_{\text{CNN}}$  is omitted.

**Two-Stage Fusion Network ( $\mathcal{G}_{\text{fuse}}$ )** This network fuses local view-dependent features with global contextual information in a two-stage MLP process. Removing this fusion step and directly feeding hierarchical features into the decoder dramatically worsens performance (PSNR: -16.27 dB, SSIM: -0.360, LPIPS: +0.374), indicating its crucial role in integrating detailed local and global context. Visual outputs without this fusion module exhibit severe deficiencies in both structure and texture (Figure 5).

## 6. Conclusion

We presented NGP-SR, a generalizable super-resolution framework for Neural Radiance Fields that reconstructs high-resolution views directly from low-resolution multi-view inputs. By combining hierarchical spatial-texture encoding, camera-aware feature integration, and global feature fusion, NGP-SR produces detail-preserving and view-consistent reconstructions. Experiments on Blender, LLFF, and DTU show that NGP-SR outperforms state-of-the-art methods, especially in challenging low-resolution settings where standard NeRF and 3DGS backbones struggle. Our framework generalizes well to unseen scenes without per-scene retraining, and ablation studies confirm the importance of each component. Our approach reconstructs high-frequency details from LR inputs, without any generative models or high-frequency cues, high-frequency signals may be challenging despite visually sharp reconstructions. Future work will extend NGP-SR to high-frequency signals, dynamic scenes and explore lighter encodings for real-time deployment.

## References

- [1] Mary Aiyetigbo, Wanqi Yuan, Feng Luo, and Nianyi Li. Implicit neural representation for video restoration. *arXiv preprint arXiv:2506.05488*, 2025. 2
- [2] Jonathan T Barron, Ben Mildenhall, Matthew Tancik, Peter Hedman, Ricardo Martin-Brualla, and Pratul P Srinivasan. Mip-nerf: A multiscale representation for anti-aliasing neural radiance fields. In *Proceedings of the IEEE/CVF international conference on computer vision*, pages 5855–5864, 2021. 1, 2
- [3] Jonathan T Barron, Ben Mildenhall, Dor Verbin, Pratul P Srinivasan, and Peter Hedman. Zip-nerf: Anti-aliased grid-based neural radiance fields. In *Proceedings of the IEEE/CVF International Conference on Computer Vision*, pages 19697–19705, 2023. 2
- [4] Anpei Chen, Zexiang Xu, Andreas Geiger, Jingyi Yu, and Hao Su. Tensorf: Tensorial radiance fields. In *European Conference on Computer Vision (ECCV)*, 2022. 5, 6
- [5] Yi-Ting Chen, Ting-Hsuan Liao, Pengsheng Guo, Alexander Schwing, and Jia-Bin Huang. Bridging diffusion models and 3d representations: A 3d consistent super-resolution framework. In *Proceedings of the IEEE/CVF International Conference on Computer Vision*, pages 13481–13490, 2025. 1, 2, 5, 7
- [6] Chao Dong, Chen C. Loy, Kaiming He, and Xiaoou Tang. Image super-resolution using deep convolutional networks. *IEEE Transactions on Pattern Analysis and Machine Intelligence*, 38:295–307, 2016. 2
- [7] Daniel Duckworth, Peter Hedman, Christian Reiser, Peter Zhizhin, Jean-François Thibert, Mario Lučić, Richard Szeliski, and Jonathan T. Barron. Smerf: Streamable memory efficient radiance fields for real-time large-scene exploration. *ACM Transactions on Graphics*, 43:63:1–63:13, 2024. 1, 2
- [8] Li Fang, Hao Zhu, Longlong Chen, Fei Hu, Long Ye, and Zhan Ma. Depth-guided bundle sampling for efficient generalizable neural radiance field reconstruction. In *CVPR*, 2025. 1, 2, 7
- [9] Jiaming Gu, Minchao Jiang, Xiaoyuan Lu, Guangming Zhu, Syed A.A. Shah, Liang Zhang, and Mohammed Bannamoun. Ue4-nerf: neural radiance field for real-time rendering of large-scale scene. In *NIPS '23: Proceedings of the 37th International Conference on Neural Information Processing Systems*, 2023. 1, 2
- [10] Yuqi Han, Tao Yu, Xiaohang Yu, Di Xu, Bing Zheng, Zonghong Dai, Changpeng Yang, Yuwang Wang, and Qionghai Dai. Super-nerf: View-consistent detail generation for nerf super-resolution. *IEEE Transactions on Visualization and Computer Graphics*, 31(9):6053–6066, 2024. 1, 2
- [11] Peter Hedman, Pratul P. Srinivasan, Ben Mildenhall, Jonathan T. Barron, and Paul Debevec. Baking neural radiance fields for real-time view synthesis. In *IEEE/CVF International Conference on Computer Vision (ICCV)*, 2021. 2
- [12] Dongting Hu, Zhenkai Zhang, Tingbo Hou, Tongliang Liu, Huan Fu, and Mingming Gong. Multiscale representation for real-time anti-aliasing neural rendering. In *IEEE/CVF International Conference on Computer Vision (ICCV)*, 2023. 2
- [13] Wenbo Hu, Yuling Wang, Lin Ma, Bangbang Yang, Lin Gao, and Xiao Liu. Tri-miprf: Tri-mip representation for efficient anti-aliasing neural radiance fields. In *IEEE/CVF International Conference on Computer Vision (ICCV)*, 2023. 2
- [14] Xudong Huang, Wei Li, Jie Hu, Hanting Chen, and Yunhe Wang. Refsr-nerf: Towards high fidelity and super resolution view synthesis. In *Proceedings of the IEEE/CVF Conference on Computer Vision and Pattern Recognition*, pages 8244–8253, 2023. 1, 2
- [15] Rasmus Jensen, Anders Dahl, George Vogiatzis, Engil Tola, and Henrik Aanaes. Large scale multi-view stereopsis evaluation. In *2014 IEEE Conference on Computer Vision and Pattern Recognition*, pages 406–413. IEEE, 2014. 5
- [16] Bernhard Kerbl, Georgios Kopanas, Thomas Leimkühler, and George Drettakis. 3d gaussian splatting for real-time radiance field rendering. *ACM Transactions on Graphics (Proceedings of ACM SIGGRAPH)*, 42(4):1–13, 2023. 2, 5, 6
- [17] Jie Long Lee, Chen Li, and Gim Hee Lee. Disr-nerf: Diffusion-guided view-consistent super-resolution nerf. In

- Proceedings of the IEEE/CVF Conference on Computer Vision and Pattern Recognition*, pages 20561–20570, 2024. 1, 2
- [18] Zhengqi Li, Simon Niklaus, Noah Snavely, and Oliver Wang. Neural scene flow fields for space-time view synthesis of dynamic scenes. In *IEEE/CVF Conference on Computer Vision and Pattern Recognition (CVPR)*, 2021. 1
- [19] Chien-Yu Lin, Qichen Fu, Thomas Merth, Karren Yang, and Anurag Ranjan. Fastsr-nerf: improving nerf efficiency on consumer devices with a simple super-resolution pipeline. In *Proceedings of the IEEE/CVF Winter Conference on Applications of Computer Vision*, pages 6036–6045, 2024. 2, 5, 6
- [20] Junchen Liu, Wenbo Hu, Zhuo Yang, Jianteng Chen, Guoliang Wang, Xiaoxue Chen, Yantong Cai, Huan-ang Gao, and Hao Zhao. Rip-nerf: Anti-aliasing radiance fields with ripmap-encoded platonic solids. In *ACM Special Interest Group on Computer Graphics and Interactive Techniques (SIGGRAPH)*, 2024. 2
- [21] Tianqi Liu, Guangcong Wang, Shoukang Hu, Liao Shen, Xinyi Ye, Yuhang Zang, Zhiguo Cao, Wei Li, and Ziwei Liu. Mvsgaussian: Fast generalizable gaussian splatting reconstruction from multi-view stereo, 2024. 1, 2, 7
- [22] Tianqi Liu, Xinyi Ye, Min Shi, Zihao Huang, Zhiyu Pan, Zhan Peng, and Zhiguo Cao. Geometry-aware reconstruction and fusion-refined rendering for generalizable neural radiance fields. In *Proceedings of the IEEE/CVF Conference on Computer Vision and Pattern Recognition (CVPR)*, pages 7654–7663, 2024. 1, 2, 7
- [23] Xianrui Luo, Huiqiang Sun, and Zhiguo Cao. Dynamic neural radiance field from defocused monocular video. In *European Conference on Computer Vision (ECCV)*, 2024. 2
- [24] Ben Mildenhall, Pratul P. Srinivasan, Rodrigo Ortiz-Cayon, Nima Khademi Kalantari, Ravi Ramamoorthi, Ren Ng, and Abhishek Kar. Local light field fusion: Practical view synthesis with prescriptive sampling guidelines. *ACM Transactions on Graphics (TOG)*, 38(4):1–14, 2019. 5
- [25] Ben Mildenhall, Pratul P Srinivasan, Matthew Tancik, Jonathan T Barron, Ravi Ramamoorthi, and Ren Ng. Nerf: Representing scenes as neural radiance fields for view synthesis. In *European Conference on Computer Vision (ECCV)*, pages 405–421, 2020. 1, 2, 5
- [26] Thomas Müller, Alex Evans, Christoph Schied, and Alexander Keller. Instant neural graphics primitives with a multiresolution hash encoding. *ACM Transactions on Graphics*, 41(4):102:1–102:15, 2022. 2, 5, 6
- [27] Seungtae Nam, Daniel Rho, Jong H. Ko, and Eunbyung Park. Mip-grid: Anti-aliased grid representations for neural radiance fields. In *NIPS '23: Proceedings of the 37th International Conference on Neural Information Processing Systems*, 2023. 2
- [28] Albert Pumarola, Enric Corona, Gerard Pons-Moll, and Francesc Moreno-Noguer. D-nerf: Neural radiance fields for dynamic scenes. In *IEEE/CVF Conference on Computer Vision and Pattern Recognition (CVPR)*, 2021. 2
- [29] Sara Rojas, Jesus Zarzar, Juan C. Pérez, Artsiom Sanakoyeu, Ali Thabet, and Albert Pumarola. Re-rend: Real-time rendering of nerfs across devices. In *IEEE/CVF International Conference on Computer Vision (ICCV)*, 2023. 2
- [30] Yuan Shen, Duygu Ceylan, Paul Guerrero, Zexiang Xu, Niloy J Mitra, Shenlong Wang, and Anna Frühstück. Supergaussian: Repurposing video models for 3d super resolution. In *European Conference on Computer Vision*, pages 215–233. Springer, 2024. 1, 2, 5, 6
- [31] Huiqiang Sun, Xingyi Li, Liao Shen, Xinyi Ye, Ke Xian, and Zhiguo Cao. Dyblurf: Dynamic neural radiance fields from blurry monocular video. In *IEEE/CVF Conference on Computer Vision and Pattern Recognition (CVPR)*, 2024. 1, 2
- [32] Yecong Wan, Mingwen Shao, Yuanshuo Cheng, and Wangmeng Zuo. S2gaussian: Sparse-view super-resolution 3d gaussian splatting, 2025. 1, 2, 5, 7
- [33] Chen Wang, Xian Wu, Yuan-Chen Guo, Song-Hai Zhang, Yu-Wing Tai, and Shi-Min Hu. Nerf-sr: High quality neural radiance fields using supersampling. In *Proceedings of the 30th ACM International Conference on Multimedia*, pages 6445–6454, 2022. 1, 2, 5, 6
- [34] Xintao Wang, Ke Yu, Shixiang Wu, Jinjin Gu, Yihao Liu, Chao Dong, Yu Qiao, and Chen C. Loy. Esrgan: Enhanced super-resolution generative adversarial networks. In *European Conference on Computer Vision (ECCV)*, 2018. 2
- [35] Xintao Wang, Liangbin Xie, Chao Dong, and Ying Shan. Real-esrgan: Training real-world blind super-resolution with pure synthetic data. In *IEEE/CVF International Conference on Computer Vision (ICCV)*, 2021. 2
- [36] Sean Wu, Shamik Basu, Tim Brodermann, Luc Van Gool, and Christos Sakaridis. Pbr-nerf: Inverse rendering with physics-based neural fields, 2025. 1
- [37] Zhiwen Yan, Chen Li, and Gim H. Lee. Nerf-ds: Neural radiance fields for dynamic specular objects. In *IEEE/CVF Conference on Computer Vision and Pattern Recognition (CVPR)*, 2023. 1, 2
- [38] Alex Yu, Ruilong Li, Matthew Tancik, Hao Li, Ren Ng, and Angjoo Kanazawa. Plenotrees for real-time rendering of neural radiance fields. In *IEEE/CVF International Conference on Computer Vision (ICCV)*, 2021. 1, 2
- [39] Zehao Yu, Anpei Chen, Binbin Huang, Torsten Sattler, and Andreas Geiger. Mip-splatting: Alias-free 3d gaussian splatting. In *Proceedings of the IEEE/CVF conference on computer vision and pattern recognition*, pages 19447–19456, 2024. 1, 2
- [40] Richard Zhang, Phillip Isola, Alexei A Efros, Eli Shechtman, and Oliver Wang. The unreasonable effectiveness of deep features as a perceptual metric. In *Proceedings of the IEEE conference on computer vision and pattern recognition*, pages 586–595, 2018. 5
- [41] Xiaoyu Zhang, Weihong Pan, Chong Bao, Xiyu Zhang, Xiaojun Xiang, Hanqing Jiang, and Hujun Bao. Lookcloser: Frequency-aware radiance field for tiny-detail scene, 2025. 1, 2